

On the Interpretation of Velocity Residuals in Protoplanetary Disks

MASATAKA AIZAWA¹ AND RYUTA ORIHARA²

¹*College of Science, Ibaraki University, 2-1-1 Bunkyo, Mito, 310-8512, Ibaraki, Japan*

²*Department of Astronomy, Graduate School of Science, The University of Tokyo, 7-3-1 Hongo, Bunkyo-ku, Tokyo 113-0033, Japan*

ABSTRACT

We present a first-order analytical model for line-of-sight velocity residuals, defined as the difference between observed velocities and those predicted by a fiducial model, assuming a flared, nearly axisymmetric disk with the perturbations in disk surface height $\delta h(r)$, inclination $\delta i(r)$, and position angle $\delta \text{PA}(r)$. Introducing projection-deprojection mapping between sky-plane and disk-frame coordinates, we demonstrate that the normalized velocity residuals exhibit Fourier components up to the third harmonic ($\sin 3\phi$ and $\cos 3\phi$). Moreover, we show that the radial profiles of $\delta h(r)$, $\delta i(r)$, and $\delta \text{PA}(r)$ can be uniquely recovered from the data by solving a linear inverse problem. For comparison, we highlight factors that are not considered in previous models. We also outline how our framework can be extended beyond the first-order residuals and applied to additional observables, such as line intensities and widths.

Keywords: Protoplanetary disks (1300)

1. INTRODUCTION

Recent ALMA observations of protoplanetary disks have revealed highly structured gas disks traced in multiple molecular lines (e.g., Öberg et al. 2021). Departures from pure Keplerian rotation could signal substructures, such as warps (e.g., Pineda et al. 2014; Casassus et al. 2015) or the presence of embedded planets (e.g., Pinte et al. 2018a, 2020). In particular, the exoALMA Large Program provides unprecedented data for studying the kinematic structure of disks (Teague et al. 2025). The survey demonstrates that disk velocity fields often display large-scale asymmetries beyond simple Keplerian profiles (Izquierdo et al. 2025; Stadler et al. 2025). Interpreting this wealth of information is essential for advancing our understanding of planet formation.

Winter et al. (2025) present an analytical model of a slightly warped disk and apply it to the exoALMA observations to explain the observed large-scale velocity residuals. In their approach, they introduce warp structures via small, radial variations in the position angle δPA and inclination δi of disk, and show that some of the observed residuals are consistent with these perturbations. Indeed, numerous protoplanetary disks show warp signatures in velocity maps (e.g., Pineda et al. 2014; Casassus et al. 2015) and in scattered-light shadows (e.g., Wagner et al. 2015; Benisty et al. 2017), although radial flows can complicate the interpretation of twisted velocity patterns for the former case (Rosenfeld et al. 2014; Zuleta et al. 2024).

However, two factors not considered in Winter et al. (2025) can substantially affect the interpretation of the observed velocity residuals. First, a rigorous treatment of the projection-deprojection mapping between sky-plane and disk-plane coordinates is essential when modeling observed velocities (e.g., Casassus & Pérez 2019). Second, the disk surface height profile, $h(r)$, and its deviation from the fiducial model, $\delta h(r)$, influence both the velocity field and the projection-deprojection mapping. Indeed, ALMA observations of disk surface emission have revealed vertical substructures (e.g., Pinte et al. 2018b; Law et al. 2021, 2022; Stapper et al. 2023), indicating that true height profiles often deviate from the simple prescriptions commonly adopted in disk modeling (e.g., Izquierdo et al. 2021). In Section 3.5, we summarize the factors that the models presented in Winter et al. (2025) do not account for.

Previously, [Casassus & Pérez \(2019\)](#) present a numerical methodology for inferring radial variations in disk structures, namely position angle, inclination, and surface height, from observed velocity fields. In this paper, we present a first-order analytical framework that computes line-of-sight velocity residuals in flared, nearly axisymmetric disks, considering the projection-deprojection mapping. Using the framework, we also present a method for recovering disk structural perturbations from observational data.

The paper is organized as follows. In Section 2, we present a general formulation for deriving velocity residuals. Section 3.1 develops the first-order expansion of these residuals. In Section 4, we discuss how we can recover $\delta h(r)$, $\delta i(r)$, $\delta \text{PA}(r)$ from the observation. Finally, Section 5 summarizes our main conclusions and discusses future prospects.

2. FORMULATION FOR VELOCITY RESIDUALS

2.1. Rotational speed

We begin by deriving the Keplerian rotation profile for a geometrically flared disk, explicitly neglecting both radial pressure gradients and disk self-gravity to isolate the purely geometric effect of the emission surface height. Deviations due to introduced by these processes are examined in [Stadler et al. \(2025\)](#) and [Longarini et al. \(2025\)](#) based on exoALMA data.

We model the motion of a fluid element of mass m located at (r, ϕ, z) in the cylindrical coordinate, where the disk surface is given by $z = h(r)$ ¹. The gravitational attraction by a central star of mass M_\star is

$$F = -\frac{GM_\star m}{R^2} \quad (1)$$

R is the distance from the central star to the fluid element.

The distance between the star and fluid element is

$$R = \sqrt{r^2 + [h(r)]^2} \quad (2)$$

Projecting the gravitational force onto the cylindrical basis $\{\hat{\mathbf{r}}, \hat{\boldsymbol{\phi}}, \hat{\mathbf{z}}\}$ gives

$$\mathbf{F} = -\frac{GM_\star m}{R^2} \left(\frac{r}{R}\right) \hat{\mathbf{r}} - \frac{GM_\star m}{R^2} \left(\frac{h}{R}\right) \hat{\mathbf{z}}, \quad (3)$$

with $\hat{\mathbf{r}} = (\cos \phi, \sin \phi, 0)$ and $\hat{\mathbf{z}} = (0, 0, 1)$.

The vertical component F_z is balanced by the disk's vertical pressure gradient, while F_r balances centrifugal force:

$$\frac{GM_\star m}{R^2} \left(\frac{r}{R}\right) = m \frac{v_\phi(r)^2}{r}. \quad (4)$$

Solving for the azimuthal velocity yields

$$v_\phi(r) = \frac{\sqrt{GM_\star} r}{(r^2 + h(r)^2)^{3/4}}. \quad (5)$$

2.2. Coordinate and line-of-sight velocity

We define coordinate frames for the sky and the disk surface following [Orihara & Momose \(2025\)](#). For the sky coordinate, we adopt a basis $\{\hat{e}_x, \hat{e}_y, \hat{e}_z\}$ defined on the celestial sphere. In this frame, \hat{e}_x points toward increasing declination (i.e. northward on the sky), \hat{e}_y points toward increasing right ascension (i.e. eastward on the sky), and \hat{e}_z

¹ Note that this variable z is used solely in the derivation of the rotational velocity and refers to the vertical height in the disk's cylindrical coordinate system. It is distinct from the z -axis later defined in the sky-frame coordinate system.

is aligned with the line of sight toward the observer (from the source to the telescope). In this sky frame, we introduce a local disk basis $\{\hat{l}, \hat{m}, \hat{n}\}$, defined by the disk's position angle (PA) and inclination i :

$$\hat{l} = (\cos \text{PA}, \sin \text{PA}, 0) \quad (6)$$

$$\hat{m} = (-\cos i \sin \text{PA}, \cos i \cos \text{PA}, -\sin i) \quad (7)$$

$$\hat{n} = (-\sin i \sin \text{PA}, \sin i \cos \text{PA}, \cos i), \quad (8)$$

where \hat{l} points along the disk major axis, \hat{n} is the unit vector normal to the disk plane (i.e., the disk axis), and \hat{m} is defined to complete the left-handed orthonormal basis.

A point on the disk surface \mathbf{S} at cylindrical coordinates (r, ϕ) and height $h(r)$ has Cartesian coordinate

$$\mathbf{S} = r(\cos \phi \hat{l} + \sin \phi \hat{m}) + r(h) \hat{n}, \quad (9)$$

$$= \begin{pmatrix} r(\cos \phi \cos \text{PA} - \cos i \sin \phi \sin \text{PA}) - h(r) \sin i \sin \text{PA} \\ r(\cos \phi \sin \text{PA} + \cos i \sin \phi \cos \text{PA}) + h(r) \sin i \cos \text{PA} \\ -r \sin i \sin \phi + h(r) \cos i \end{pmatrix}, \quad (10)$$

where only the upper surface is considered. Here we measure the azimuthal angle ϕ from the major axis $\phi = 0$ in the disk plane: $\phi = \pi/2$ corresponds to the far side of the upper surface (farthest from the observer), while $\phi = 3\pi/2$ corresponds to the near side. The unit vector in the azimuthal direction is

$$\hat{e}_\phi = (-\sin \phi \hat{l} + \cos \phi \hat{m}), \quad (11)$$

Assuming all emission arises from this upper layer, the line-of-sight velocity is

$$v_{\text{los}}(r, \phi) = (-1)^\varepsilon |v_\phi(r) [\hat{e}_\phi \cdot \hat{e}_z]| \quad (12)$$

$$= (-1)^\varepsilon \frac{\sqrt{GM_\star} r}{(r^2 + h(r)^2)^{3/4}} \sin i \cos \phi \quad (13)$$

where the direction of the disk rotation is specified by ε :

$$\varepsilon = \begin{cases} 0, & \text{if rotation is counterclockwise to the observer,} \\ 1, & \text{if rotation is clockwise to the observer,} \end{cases} \quad (14)$$

When $\varepsilon = 1$, $\phi = 0$ corresponds to the blue-shifted direction, whereas when $\varepsilon = 0$, $\phi = 0$ corresponds to the red-shifted direction.

2.3. True and approximate models

To interpret the observed velocity residuals, we introduce two disk-geometry models:

Model 0 (approximate): The fiducial geometry used to fit the data,

$$\{h_0(r), i_0, \text{PA}_0\}. \quad (15)$$

Model 1 (true): The actual disk geometry,

$$\{h(r), i(r), \text{PA}(r)\} = \{h_0(r) + \delta h(r), i_0 + \delta i(r), \text{PA}_0 + \delta \text{PA}(r)\}. \quad (16)$$

Unless otherwise stated, in the majority of expressions we drop the (r) argument and denote

$$(\delta h(r), \delta i(r), \delta \text{PA}(r)) \rightarrow (\delta h, \delta i, \delta \text{PA}). \quad (17)$$

The measured velocity field follows Model 1, whereas Model 0 represents the best-fit geometry. We define

$$v_{\text{los},0}(r, \phi) \equiv v_{\text{los}}(r, \phi | h_0(r), \text{PA}_0, i_0) \quad (18)$$

$$v_{\text{los},\delta}(r, \phi) \equiv v_{\text{los}}(r, \phi | h_0(r) + \delta h, i_0 + \delta i, \text{PA}_0 + \delta \text{PA}). \quad (19)$$

As discussed later, the observed velocity residuals do not correspond to the simple difference of the two model fields $v_{\text{los},\delta}(r, \phi) - v_{\text{los},0}(r, \phi)$, as is assumed in Winter et al. (2025).

2.4. Deprojection/Projection mapping

We define projection and deprojection mapping between the sky-plane coordinates (x, y) and the disk-plane coordinates (r, ϕ) :

$$(x, y) = \mathcal{P}_{h(r), i, \text{PA}}(r, \phi) \quad (\text{projection onto the sky plane}), \quad (20)$$

$$(r, \phi) = \mathcal{P}_{h(r), i, \text{PA}}^{-1}(x, y) \quad (\text{deprojection onto the disk plane}). \quad (21)$$

These projection and deprojection operators are conceptually equivalent to $\mathbf{f}_{\text{PA}, i, +\psi}$ and $\mathbf{f}_{\text{PA}, i, +\psi}^{-1}$ in Casassus & Pérez (2019) where ψ denotes the opening angle function for the disk, although the definitions of coordinates, functions, and parameters differ.

For a highly inclined disk with a large height function, the projection mapping \mathcal{P} can be non-injective, so that distinct (r, ϕ) may map to the same sky-plane coordinate (x, y) , in contrast to the statement in Casassus & Pérez (2019). In other words, the deprojection mapping \mathcal{P}^{-1} can be multi-valued: \mathcal{P}^{-1} may yield multiple (r, ϕ) solutions. Nevertheless, for simplicity we assume that \mathcal{P} is injective, so that each (x, y) corresponds uniquely to a single (r, ϕ) .

From Equation (10), the projection onto the sky plane is

$$x = r(\cos \phi \cos \text{PA} - \cos i \sin \phi \sin \text{PA}) - h(r) \sin i \sin \text{PA} \quad (22)$$

$$y = r(\cos \phi \sin \text{PA} + \cos i \sin \phi \cos \text{PA}) + h(r) \sin i \cos \text{PA} \quad (23)$$

Since the projection depends on the assumed geometry, we introduce

$$\mathcal{P}_0 \equiv \mathcal{P}_{h_0(r), i_0, \text{PA}_0}, \quad (24)$$

$$\mathcal{P}_\delta \equiv \mathcal{P}_{h_0(r)+\delta h, i_0+\delta i, \text{PA}_0+\delta \text{PA}}, \quad (25)$$

for Model 0 (approximate) and Model 1 (true), respectively.

2.5. Velocity residuals in observation

In the ideal (noise-free) case without beam smearing, the measured velocity field $v_{\text{obs}}(x, y)$ equals the true line-of-sight velocity evaluated with the true disk coordinate, i.e.

$$v_{\text{obs}}(x, y) = v_{\text{los}, \delta}(r, \phi), \quad (x, y) = \mathcal{P}_\delta(r, \phi). \quad (26)$$

Here $v_{\text{los}, \delta}(r, \phi)$ and \mathcal{P}_δ refer to the “true” geometry (Model 1). Note that the disk coordinate (r, ϕ) themselves depend on \mathcal{P}_δ ; observers only know $v_{\text{obs}}(x, y)$ and must infer \mathcal{P}_δ .

By contrast, the modeled velocity field uses the fiducial (Model 0) geometry:

$$v_{\text{Model 0}}(x, y) = v_{\text{los}, 0}(r, \phi), \quad (x, y) = \mathcal{P}_0(r, \phi). \quad (27)$$

Thus, the velocity residual in the sky plane $\delta v_{\text{obs}}(x, y)$ resulting from fitting the model to the data can be expressed as:

$$\delta v_{\text{obs}}(x, y) = v_{\text{obs}}(x, y) - v_{\text{Model 0}}(x, y) \quad (28)$$

$$= v_{\text{los}, \delta}(\mathcal{P}_\delta^{-1}(x, y)) - v_{\text{los}, 0}(\mathcal{P}_0^{-1}(x, y)) \quad (29)$$

$$= [v_{\text{los}, \delta}(\mathcal{P}_\delta^{-1}(x, y)) - v_{\text{los}, \delta}(\mathcal{P}_0^{-1}(x, y))] + [v_{\text{los}, \delta}(\mathcal{P}_0^{-1}(x, y)) - v_{\text{los}, 0}(\mathcal{P}_0^{-1}(x, y))]. \quad (30)$$

Here, the first term represents the error introduced by deprojection (mapping error), while the second term represents the difference in the functional form of v_{los} .

In the realistic situation, one deprojects the observed velocity using the fiducial model:

$$v_{\text{obs, depro}}(r, \phi) = v_{\text{obs}}(x, y), \quad (r, \phi) = \mathcal{P}_0^{-1}(x, y), \quad (31)$$

Using Equation (26) we obtain

$$v_{\text{obs,depro}}(r, \phi) = v_{\text{los},\delta}(\mathcal{P}_\delta^{-1}(\mathcal{P}_0(r, \phi))) \quad (32)$$

Similarly, the deprojected fiducial model is

$$v_{0,\text{depro}}(r, \phi) = v_{\text{los},0}(\mathcal{P}_0^{-1}(\mathcal{P}_0(r, \phi))) = v_{\text{los},0}(r, \phi). \quad (33)$$

Therefore, the residual in disk coordinates is

$$\delta v_{\text{obs,depro}}(r, \phi) = v_{\text{obs,depro}}(r, \phi) - v_{0,\text{depro}}(r, \phi) \quad (34)$$

$$= v_{\text{los},\delta}(\mathcal{P}_\delta^{-1}(\mathcal{P}_0(r, \phi))) - v_{\text{los},0}(r, \phi) \quad (35)$$

$$= \underbrace{[v_{\text{los},\delta}(\mathcal{P}_\delta^{-1}(\mathcal{P}_0(r, \phi))) - v_{\text{los},\delta}(r, \phi)]}_{\text{mapping error}} + \underbrace{[v_{\text{los},\delta}(r, \phi) - v_{\text{los},0}(r, \phi)]}_{\text{model difference}} \quad (36)$$

Similar to Equation (30), the first term corresponds to the (projection-deprojection) mapping error, while the second term corresponds to the functional difference in v_{los} .

In the next section we expand Equation (36) to first order in the small perturbations ($\delta h, \delta i, \delta \text{PA}$). The deprojected velocity residual $\delta v_{\text{res,depro}}(r, \phi)$ can be mapped back to sky-plane coordinates simply by applying the fiducial projection operator $\mathcal{P}_0(r, \phi)$. Since $\delta v_{\text{res,depro}}$ is already $\mathcal{O}(\delta)$, any error from using \mathcal{P}_0 instead of the exact projection is only $\mathcal{O}(\delta^2)$ and can be neglected.

3. FIRST-ORDER EXPANSION OF VELOCITY RESIDUAL AND ITS RETRIEVAL FROM OBSERVATION

3.1. Mapping-error and model-difference terms

We expand Equation (36) to first order in the perturbations ($\delta h, \delta i, \delta \text{PA}$). As noted above, the total residual in Equation (36) naturally decomposes into two contributions: a mapping-error term, which captures projectiondeprojection mismatches, and the model-difference term. The model-difference contribution is then given by:

$$v_{\text{los},\delta}(r, \phi) - v_{\text{los},0}(r, \phi) = \left(\frac{\partial v_{\text{los}}}{\partial i} \right) \delta i + \left(\frac{\partial v_{\text{los}}}{\partial h} \right) \delta h + \left(\frac{\partial v_{\text{los}}}{\partial \text{PA}} \right) \delta \text{PA} + \mathcal{O}(\delta^2) \quad (37)$$

$$= (-1)^\epsilon [V_{K,0}(r) \cot i_0 \cos \phi] \delta i - (-1)^\epsilon \left[V_{K,0}(r) \left(\frac{3h_0(r)h'_0(r)}{2(r^2 + h_0^2(r))} \right) \cos \phi \right] \delta h + \mathcal{O}(\delta^2), \quad (38)$$

where we define

$$V_{K,0}(r) = \frac{\sqrt{GM_\star} r}{(r^2 + h_0(r)^2)^{3/4}} \sin i_0. \quad (39)$$

To compute the mapping error, we define small shifts δr and $\delta \phi$ by

$$\mathcal{P}_\delta^{-1}(\mathcal{P}_0(r, \phi)) = (r + \delta r, \phi + \delta \phi). \quad (40)$$

Then, the mapping error can be computed as:

$$v_{\text{los},\delta}(\mathcal{P}_\delta^{-1}(\mathcal{P}_0(r, \phi))) - v_{\text{los},\delta}(r, \phi) = v_{\text{los},\delta}(r + \delta r, \phi + \delta \phi) - v_{\text{los},\delta}(r, \phi) \quad (41)$$

$$= \left(\frac{\partial v_{\text{los},\delta}}{\partial r} \right) \delta r + \left(\frac{\partial v_{\text{los},\delta}}{\partial \phi} \right) \delta \phi + \mathcal{O}(\delta^2) \quad (42)$$

$$= \left(\frac{\partial v_{\text{los},0}}{\partial r} \right) \delta r + \left(\frac{\partial v_{\text{los},0}}{\partial \phi} \right) \delta \phi + \mathcal{O}(\delta^2), \quad (43)$$

where one finds

$$\frac{\partial v_{\text{los},0}}{\partial r} = -(-1)^\epsilon V_{K,0}(r) A(r) \cos \phi \quad (44)$$

$$\frac{\partial v_{\text{los},0}}{\partial \phi} = -(-1)^\epsilon V_{K,0}(r) \sin \phi \quad (45)$$

$$A(r) \equiv \left(\frac{r + 3h_0(r)h'_0(r) - 2h_0^2(r)/r}{2(r^2 + h_0^2(r))} \right) \quad (46)$$

Adding Equations (38) and (43) gives the full first-order expansion of Equation (36).

3.2. Calculation of $\delta r, \delta \phi$ due to mapping error

To compute $(\delta r, \delta \phi)$ in Equation (52), induced by perturbation in $(\delta h, \delta i, \delta \text{PA})$, we define the projection functions

$$f(r, \phi, h(r), \text{PA}, i) \equiv x = r(\cos \phi \cos \text{PA} - \cos i \sin \phi \sin \text{PA}) - h(r) \sin i \sin \text{PA}, \quad (47)$$

$$g(r, \phi, h(r), \text{PA}, i) \equiv y = r(\cos \phi \sin \text{PA} + \cos i \sin \phi \cos \text{PA}) + h(r) \sin i \cos \text{PA}. \quad (48)$$

Taking the total differentials of f and g , we find:

$$df = f_r \delta r + f_\phi \delta \phi + f_h \delta h + f_i \delta i + f_{\text{PA}} \delta \text{PA} \quad (49)$$

$$dg = g_r \delta r + g_\phi \delta \phi + g_h \delta h + g_i \delta i + g_{\text{PA}} \delta \text{PA} \quad (50)$$

Fixing (x, y) on the sky coordinate, we obtain

$$df = dx = 0, \quad dg = dy = 0 \quad (51)$$

Combining Equation (47), (48), and (51), we find

$$\begin{pmatrix} \delta r \\ \delta \phi \end{pmatrix} = -\frac{1}{f_r g_\phi - f_\phi g_r} \begin{pmatrix} g_\phi & -f_\phi \\ -g_r & f_r \end{pmatrix} \begin{pmatrix} f_h & f_i & f_{\text{PA}} \\ g_h & g_i & g_{\text{PA}} \end{pmatrix} \begin{pmatrix} \delta h \\ \delta i \\ \delta \text{PA} \end{pmatrix}, \quad (52)$$

Equivalently, we have

$$\delta r = \left(\frac{\partial r}{\partial h} \right) \delta h + \left(\frac{\partial r}{\partial i} \right) \delta i + \left(\frac{\partial r}{\partial \text{PA}} \right) \delta \text{PA} \quad (53)$$

$$\delta \phi = \left(\frac{\partial \phi}{\partial h} \right) \delta h + \left(\frac{\partial \phi}{\partial i} \right) \delta i + \left(\frac{\partial \phi}{\partial \text{PA}} \right) \delta \text{PA} \quad (54)$$

$$r_p \equiv \frac{\partial r}{\partial p} = \frac{f_\phi g_p - g_\phi f_p}{f_r g_\phi - f_\phi g_r}, \quad \phi_p \equiv \frac{\partial \phi}{\partial p} = \frac{g_r f_p - f_r g_p}{f_r g_\phi - f_\phi g_r} \quad (p = h, \text{PA}, i). \quad (55)$$

Here, subscripts indicate partial derivatives, e.g.

$$f_r \equiv \frac{\partial f}{\partial r} \quad (56)$$

In Appendix (A.1), we show derivations of $f_r, f_\phi, g_r, g_\phi, r_p, \phi_p$.

For convenience, we define the denominator for r_p and ϕ_p in Equation (55) as

$$\Delta = \Delta(r, \phi) \equiv f_r g_\phi - f_\phi g_r = r(\cos i_0 + h'_0(r) \sin i_0 \sin \phi). \quad (57)$$

The mapping $(r, \phi) \rightarrow (x, y)$ becomes singular when $\Delta = 0$, i.e. when

$$h'_0(r) \sin i_0 \sin \phi = -\cos i_0, \quad (58)$$

which corresponds to the line of sight being tangent to the flared surface (the “rim”). Although this can occur for inclined or strongly flared disks, for each r there are at most two solutions in $\phi \in [0, 2\pi)$, so the singular locus has measure zero and may be ignored. We therefore assume $\Delta \neq 0$ in what follows.

3.3. First-order expansion of velocity residuals

Using Equation (52), the deprojection (mapping)-error term in Equation (43) can be written as

$$[v_{\text{los},\delta}(\mathcal{P}_\delta^{-1}(\mathcal{P}_0(r, \phi))) - v_{\text{los},\delta}(r, \phi)] \quad (59)$$

$$= (-1)^{\varepsilon+1} \frac{V_{K,0}(r)}{\Delta(r, \phi)} \Delta \left[\left(\frac{\partial r}{\partial h} \delta h + \frac{\partial r}{\partial i} \delta i + \frac{\partial r}{\partial \text{PA}_0} \delta \text{PA}_0 \right) A(r) \cos \phi + \left(\frac{\partial \phi}{\partial h} \delta h + \frac{\partial \phi}{\partial i} \delta i + \frac{\partial \phi}{\partial \text{PA}_0} \delta \text{PA}_0 \right) \sin \phi \right] + \mathcal{O}(\delta^2) \quad (60)$$

$$= (-1)^{\varepsilon+1} \frac{V_{K,0}(r)}{\Delta(r, \phi)} [B(r, \phi) \delta h + C(r, \phi) \delta i + D(r, \phi) \delta \text{PA}] + \mathcal{O}(\delta^2) \quad (61)$$

where we summarize the terms using

$$B(r, \phi) = B_0(r) \sin 2\phi, \quad (62)$$

$$C(r, \phi) = C_0(r) \cos \phi + C_1(r) \sin 2\phi + C_2(r) \cos 3\phi, \quad (63)$$

$$D(r, \phi) = D_0(r) + D_1(r) \sin \phi + D_2(r) \cos 2\phi + D_3(r) \sin 3\phi. \quad (64)$$

The detailed functional forms for the coefficients $B_i(r), C_i(r), D_i(r)$ are presented in Appendix A.2.

Finally, combining Equations (38) and (61), we obtain the velocity residuals in Equation (36):

$$\delta v_{\text{obs,depro}}(r, \phi) = [v_{\text{los},\delta}(\mathcal{P}_\delta^{-1}(\mathcal{P}_0(r, \phi))) - v_{\text{los},\delta}(r, \phi)] + [v_{\text{los},\delta}(r, \phi) - v_{\text{los},0}(r, \phi)] \quad (65)$$

$$= (-1)^{\varepsilon+1} \frac{V_{K,0}(r)}{\Delta(r, \phi)} \left[B(r, \phi) \delta h + C(r, \phi) \delta i + D(r, \phi) \delta \text{PA} - [\Delta(r, \phi) \cot i_0 \cos \phi] \delta i + \left[\Delta(r, \phi) \left(\frac{3h_0(r)}{r^2 + h_0^2(r)} \right) \cos \phi \right] \delta h \right] + \mathcal{O}(\delta^2), \quad (66)$$

We then decompose the last two terms as

$$-\Delta(r, \phi) \cot i_0 \cos \phi = E_0(r) \cos \phi + E_1(r) \sin 2\phi \quad (67)$$

$$\Delta(r, \phi) \left(\frac{3h_0(r)}{2(r^2 + h_0^2(r))} \right) \cos \phi = F_0(r) \cos \phi + F_1(r) \sin 2\phi. \quad (68)$$

The detailed functional forms for $E_i(r), F_i(r)$ are presented in Appendix A.2.

Multiplying Equation (66) by $(-1)^{\varepsilon+1} \Delta/V_{K,0}$ then gives

$$\begin{aligned} (-1)^{\varepsilon+1} \frac{\delta v_{\text{res,depro}}(r, \phi) \Delta(r, \phi)}{V_{K,0}(r)} &= [F_0(r) \cos \phi + (B_0(r) + F_1(r)) \sin 2\phi] \delta h \\ &+ [(C_0(r) + E_0(r)) \cos \phi + (C_1(r) + E_1(r)) \sin 2\phi + C_2(r) \cos 3\phi] \delta i \\ &+ [D_0(r) + D_1(r) \sin \phi + D_2(r) \cos 2\phi + D_3(r) \sin 3\phi] \delta \text{PA} + \mathcal{O}(\delta^2). \end{aligned} \quad (69)$$

The equivalent Fourier-series expansion is given in Appendix A.3.

In Equation (69), the quantities on the left-hand side can be computed directly from the observational data and the fiducial model, while the coefficients on the right-hand side are determined entirely by the fiducial geometry. Hence, one can invert Equation (69) to recover $\delta h(r)$, $\delta i(r)$, and $\delta \text{PA}(r)$, as described in Section 4.

3.4. Comparison of numerical calculation and analytical solution

To validate our analytical model, we compare its predictions with numerically computed velocity fields, adopting the J1615 disk from the exoALMA survey (Teague et al. 2025) as our fiducial case. We set

$$M_\star = 1.14 M_\odot, i_0 = 45^\circ, \text{PA}_0 = -90^\circ, \varepsilon = 1, \quad (70)$$

where PA is taken to be -90° for visualization. Here, the west side is blue-shifted and the azimuthal angle ϕ is measured counter-clockwise from the blue-shifted major axis. We assume a flared surface assuming radial range $r \in [30, 600]$ au:

$$h(r) = z_0 \left(\frac{r}{D_0} \right)^p \exp[-(r/R_t)^q] \quad (71)$$

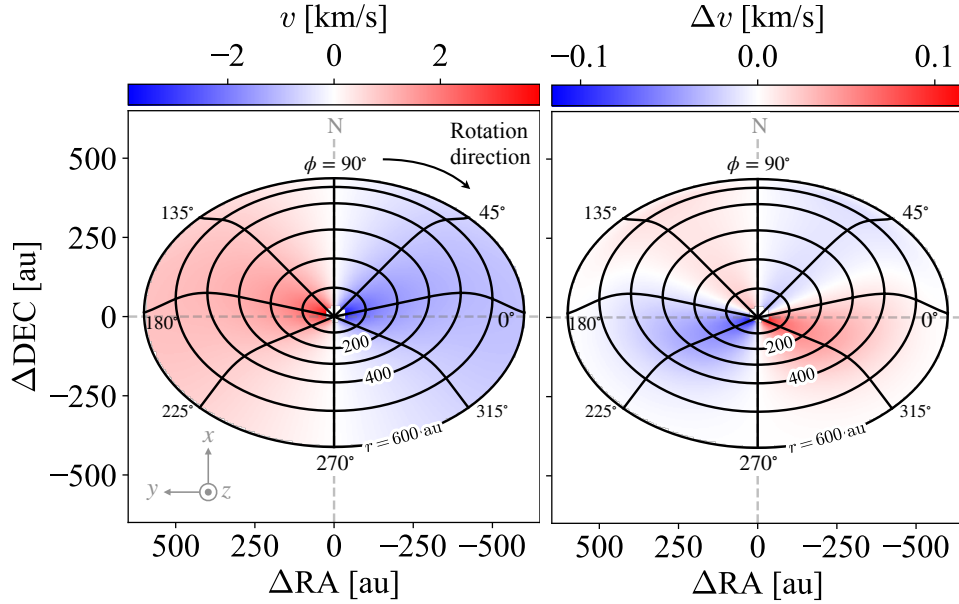


Figure 1. Sky-plane line-of-sight velocity (left) and residuals (right) from numerical calculations for a height perturbation of $\delta h(r) = 0.1 h(r)$.

with parameters for ^{12}CO from Izquierdo et al. (2025):

$$z_0 = 26.3 \text{ au}, D_0 = 100 \text{ au}, p = 1.04, R_t = 530 \text{ au}, q = 6.89. \quad (72)$$

Its derivative is given by

$$h'(r) = h(r) \left[p/r - (q/R_t)(r/R_t)^{q-1} \right]. \quad (73)$$

We impose a perturbation

$$\delta h(r) = 0.1 h(r), \delta i = 1^\circ, \delta \text{PA} = 1^\circ \quad (74)$$

and compute two velocity fields for Model 0 (approximate) and Model 1 (true). In our numerical calculations, we project each field onto the sky plane via the operator \mathcal{P} , using the corresponding geometry. We then compute the residuals between the two projected models and deproject them back into the disk-plane coordinate system (also see Section 2.5).

Figure 1 shows the numerically computed velocity fields and residuals, defined as the difference between Model 1 (true) and Model 0 (approximate), in the projected frame. The models differ by a perturbation in disk surface height, with $\delta h(r) = 0.1 h(r)$ applied in Model 1. Figure 2 compare the numerically computed velocity residuals with the analytical predictions in the deprojected frame for perturbations in δh , δi , and δPA . The excellent agreement confirms the validity of the analytical model presented here. Figure 3 plots the radial profiles of the harmonic coefficients, alongside $h_0(r)$ and $h'_0(r)$. On average, the $\sin 2\phi$, $\cos \phi$, and $\sin \phi$ Fourier modes dominate the δh , δi , and δPA signals, respectively; nevertheless, each perturbation contains additional harmonics that give rise to more intricate residual patterns.

3.5. Comments on previous models in Winter et al. (2025)

We reexamine the analytic approach of Winter et al. (2025). They begin from the line-of-sight velocity

$$v_{\text{los}}(r, \phi) = \sqrt{\frac{GM_\star}{r}} \sin i \cos(\phi - \text{PA}), \quad (75)$$

setting $h(r) = 0$ and linearize in $\delta i, \delta \text{PA}$ to obtain

$$\delta v = \sqrt{\frac{GM_\star}{r}} (\cos i \cos(\phi - \text{PA}) \delta i + \sin i \sin(\phi - \text{PA}) \delta \text{PA}). \quad (76)$$

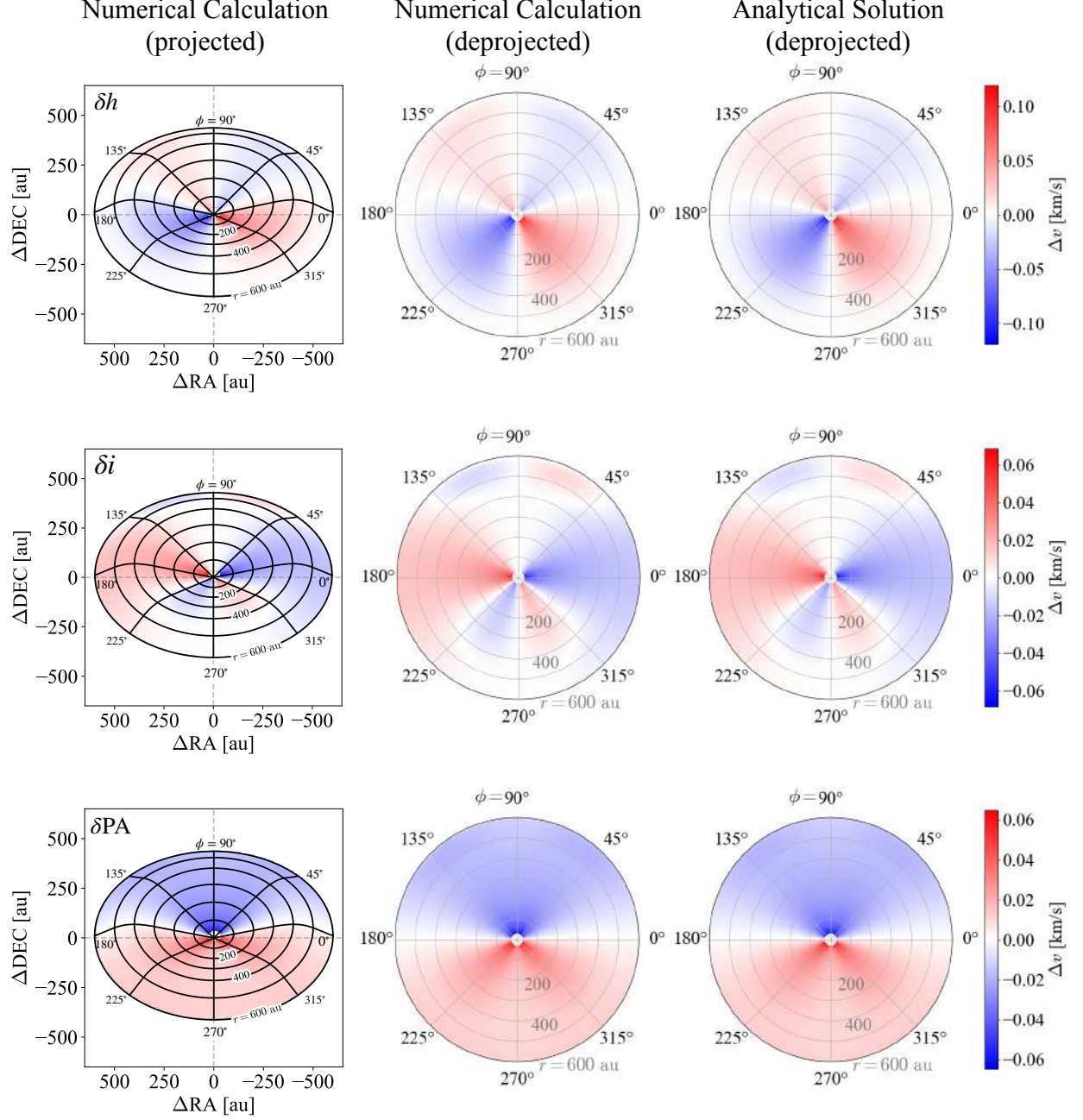


Figure 2. Comparison of line-of-sight velocity residuals from numerical calculation (left column) and analytical solution (right column) for three perturbations: $\delta h(r) = 0.1 h(r)$ (top row), $\delta i = 1^\circ$ (middle row), and $\delta PA = 1^\circ$ (bottom row).

However, PA denotes a rotation of the sky-plane frame and is not part of the disk-plane azimuth ϕ , so it is, strictly speaking, incorrect to use $\cos(\phi - PA)$. While Winter et al. (2025) set $PA = 0$ assuming “without loss of generality”, which reduces the expression to $\cos \phi$ as in our study, the use of $(\phi - PA)$ still introduces an unintended $\partial/\partial PA$ term in Equation (76). Although δPA does produce a $\sin \phi$ via mapping errors in our model, this effect is distinct from the derivative of $\cos(\phi - PA)$ in Winter et al. (2025).

Winter et al. (2025) also neglect errors arising from the projection-deprojection mapping. Even when $h(r) = h'(r) = 0$ as in Winter et al. (2025), the deprojection generates coefficients $C_0(r)$, $C_2(r)$, $D_1(r)$, and $D_3(r)$ with $A(r)$ being $1/2r$.

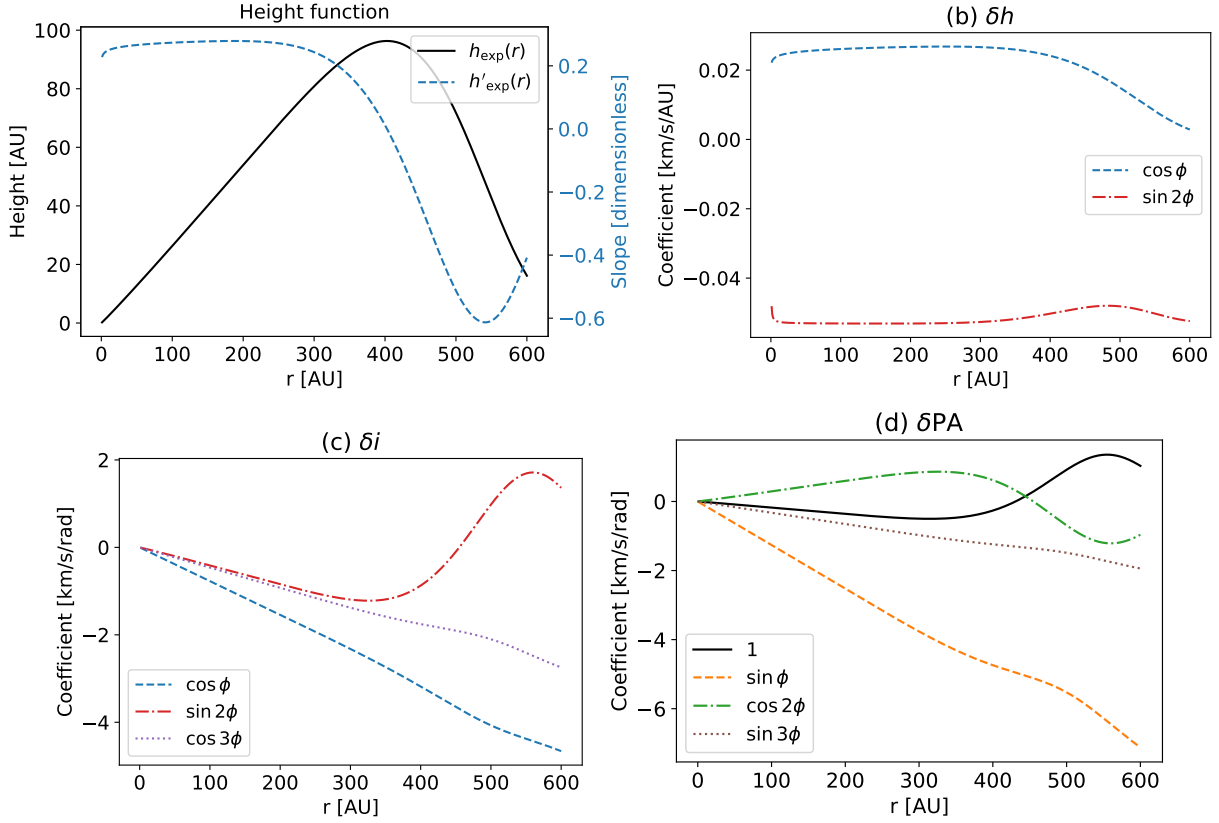


Figure 3. (Upper-left) Fiducial disk surface height profile $h_0(r)$ (solid) and its radial derivative $h'_0(r)$ (dashed). (Others) Radial profiles of the key Fourier coefficients in Equation (69) for perturbations in (b) disk height $\delta h(r)$, (c) inclination δi , and (d) position angle δPA .

These neglected contributions produce azimuthal harmonics with $m = 1 - 3$ that are non-negligible, and in particular the $m = 1$ components have amplitudes that differ from those adopted by Winter et al. (2025).

These factors can qualitatively alter the interpretation of the observed velocity fields. Moreover, variations in the disk surface height, not considered in Winter et al. (2025), can introduce significant residuals. Although Winter et al. (2025) make the important contribution of introducing a perturbative expansion of velocity residuals in protoplanetary disks, a comprehensive reanalysis of their exoALMA results is warranted to ensure an accurate interpretation of the observational data.

4. ON DETERMINATION OF DISK STRUCTURE FROM OBSERVATION

The left-hand side of Equation (69), is constructed entirely from the observables and the fiducial model once its parameters are fitted. We therefore can expand it in a Fourier series:

$$(-1)^{\varepsilon+1} \frac{\Delta(r, \phi) \delta v_{\text{res,depro}}(r, \phi)}{V_{K,0}(r)} = a_0(r) + \sum_{n=1}^3 [a_n(r) \cos n\phi + b_n(r) \sin n\phi]. \quad (77)$$

Comparing with Equation (69), we obtain at each radius r :

$$\begin{pmatrix} a_0(r) \\ a_1(r) \\ a_2(r) \\ a_3(r) \\ b_1(r) \\ b_2(r) \\ b_3(r) \end{pmatrix} = \mathbf{X}(r) \begin{pmatrix} \delta h(r) \\ \delta i(r) \\ \delta \text{PA}(r) \end{pmatrix} \quad (78)$$

where we define the design matrix $\mathbf{X}(r)$:

$$\mathbf{X}(r) \equiv \begin{pmatrix} 0 & 0 & D_0(r) \\ F_0(r) & C_0(r) + E_0(r) & 0 \\ 0 & 0 & D_2(r) \\ 0 & C_2(r) & 0 \\ 0 & 0 & D_1(r) \\ B_0(r) + F_1(r) & C_1(r) + E_1(r) & 0 \\ 0 & 0 & D_3(r) \end{pmatrix}. \quad (79)$$

The set of basis functions for the coefficients is $[1, \cos \phi, \cos 2\phi, \cos 3\phi, \sin \phi, \sin 2\phi, \sin 3\phi]$. By performing a least-squares fit at each r , the point estimates are

$$\begin{pmatrix} \hat{\delta h}(r) \\ \hat{\delta i}(r) \\ \widehat{\delta \text{PA}}(r) \end{pmatrix} = [\mathbf{X}(r)^T \mathbf{X}(r)]^{-1} \mathbf{X}(r)^T \begin{pmatrix} a_0(r) \\ a_1(r) \\ a_2(r) \\ a_3(r) \\ b_1(r) \\ b_2(r) \\ b_3(r) \end{pmatrix}. \quad (80)$$

Beyond these point-estimates, one can derive posterior distributions for the perturbation profiles $(\delta h(r_i), \delta i(r_i), \delta \text{PA}(r_i))$ by assuming (possibly correlated) Gaussian noise on the measured Fourier coefficients and placing a Gaussian-process prior to model radial correlations. Because the problem is linear in the perturbations, the posterior can be obtained in an analytical framework (up to GP hyperparameters) (e.g., Aizawa et al. 2024).

5. CONCLUSION AND DISCUSSION

We present a first-order analytical model for line-of-sight velocity residuals in flared, nearly axisymmetric disks subject to small perturbations $(\delta h(r), \delta i(r), \delta \text{PA}(r))$. By accounting for both projection and deprojection, we show that the normalized residual field, derivable from observations and the fiducial model, decomposes into azimuthal harmonics up to $m = 3$. We also present the framework for recovering the perturbation profiles $\delta h(r)$, $\delta i(r)$ and $\delta \text{PA}(r)$ from the data. The warped-disk model employed by Winter et al. (2025) is susceptible to inaccuracies arising from simplified assumptions, and the reanalysis of the exoALMA data within our framework would thus enable more reliable interpretation.

In this work, we adopt an idealized, noise-free case without beam smearing and assume that emission originates exclusively from the upper disk surface; however, neither assumption holds in real observations. We also neglect radial pressure-gradient corrections or self-gravity terms (e.g., Pinte et al. 2018a; Longarini et al. 2025; Stadler et al. 2025),

which alter the azimuthal velocity profile, as well as any radial or vertical flow components (Rosenfeld et al. 2014; Teague et al. 2019; Zuleta et al. 2024).

Several extensions to our model are possible. First, allowing the fiducial inclination and position angle to vary with radius, $i_0(r)$ and $\text{PA}_0(r)$, and iteratively updating $[h_0(r), i_0(r), \text{PA}_0(r)] \rightarrow [h_0(r) + \delta h(r), i_0(r) + \delta i(r), \text{PA}_0(r) + \delta \text{PA}(r)]$ would enable convergence to the true geometry even in strongly warped disks. This requires adding the corresponding partial derivatives of $i(r)$ and $\text{PA}(r)$ in the expressions for f_r and g_r in Equations (A1) and (A2) and all subsequent terms. Second, our perturbative framework can be applied to other observables, such as line intensities or widths, as functions of (r, ϕ) by replacing the partial derivatives in Equations (37) and (43) accordingly. The velocity fields can be also modified to incorporate pressure-gradient corrections, self-gravity terms, and vertical motions. Such extensions would enable a more robust inference of disk parameters and the identification of non-axisymmetric features (e.g. spirals). We leave them to future work.

ACKNOWLEDGEMENTS

We acknowledge fruitful discussions with Munetake Momose. This work was supported by JSPS KAKENHI grant number 25K17431. We acknowledge the use of ChatGPT (GPT-4o; OpenAI) for grammatical and clarity improvements throughout the manuscript.

APPENDIX

A. EXPLICIT EXPRESSIONS FOR DERIVATIVES AND COEFFICIENTS

A.1. Derivatives of f and g with respect to r , ϕ , h , i , and PA

Each term in Equation (55) with respect to r, ϕ derivatives is given by:

$$f_r = (\cos \phi \cos \text{PA}_0 - \cos i_0 \sin \phi \sin \text{PA}_0) - h'_0(r) \sin i_0 \sin \text{PA}_0, \quad f_\phi = -r(\sin \phi \cos \text{PA}_0 + \cos i_0 \cos \phi \sin \text{PA}_0), \quad (\text{A1})$$

$$g_r = (\cos \phi \sin \text{PA}_0 + \cos i_0 \sin \phi \cos \text{PA}_0) + h'_0(r) \sin i_0 \cos \text{PA}_0, \quad g_\phi = r(-\sin \phi \sin \text{PA}_0 + \cos i_0 \cos \phi \cos \text{PA}_0) \quad (\text{A2})$$

The each of term in Equation (55) with respect to h, i, PA derivatives is given by:

$$f_h = -\sin i_0 \sin \text{PA}_0, \quad f_{\text{PA}} = -r(\cos \phi \sin \text{PA}_0 + \cos i_0 \sin \phi \cos \text{PA}_0) - h_0(r) \sin i_0 \cos \text{PA}_0, \quad (\text{A3})$$

$$f_i = r \sin i_0 \sin \phi \sin \text{PA}_0 - h_0(r) \cos i_0 \sin \text{PA}_0, \quad (\text{A4})$$

$$g_h = \sin i_0 \cos \text{PA}_0, \quad g_{\text{PA}} = r(\cos \phi \cos \text{PA}_0 - \cos i_0 \sin \phi \sin \text{PA}_0) - h_0(r) \sin i_0 \sin \text{PA}_0, \quad (\text{A5})$$

$$g_i = -r \sin i_0 \sin \phi \cos \text{PA}_0 + h_0(r) \cos i_0 \cos \text{PA}_0. \quad (\text{A6})$$

In addition, we find:

$$r_h \Delta = -r \sin i_0 \sin \phi, \quad \phi_h \Delta = -\sin i_0 \cos \phi, \quad r_i \Delta = -r \sin \phi (h_0(r) \cos i_0 - r \sin i_0 \sin \phi) \quad (\text{A7})$$

$$\phi_i \Delta = r \sin i_0 \cos \phi \sin \phi - h_0(r) \cos i_0 \cos \phi, \quad r_{\text{PA}_0} \Delta = -r \cos \phi \sin i_0 (r \sin \phi \sin i_0 - h \cos i_0) \quad (\text{A8})$$

$$\phi_{\text{PA}_0} \Delta = -h_0(r) \sin i_0 (h'_0(r) \sin i_0 + \cos i_0 \sin \phi) - r h'_0(r) \sin i_0 \cos i_0 \sin \phi - r(\cos^2 \phi + \cos^2 i_0 \sin^2 \phi) \quad (\text{A9})$$

A.2. Explicit forms of $B_i(r)$ - $F_i(r)$

The explicit functional forms of the coefficients for $B_i(r)$ - $F_i(r)$ are

$$B_0(r) = - \left[\frac{\sin i_0 (rA(r) + 1)}{2} \right], \quad C_0(r) = \left[\frac{r + r^2 A(r)}{4} \right] \sin i_0, \quad C_1(r) = - \left[\frac{1 + rA(r)}{2} \right] h_0(r) \cos i_0 \quad (\text{A10})$$

$$C_2(r) = - \left[\frac{(1 + rA(r))}{4} \right] r \sin i_0, \quad D_0(r) = \frac{\sin i_0 \cos i}{2} [rA(r)h_0(r) - h_0(r) - rh'_0(r)], \quad (\text{A11})$$

$$D_1(r) = -h_0(r)h'_0(r) \sin^2 i_0 - \frac{r^2 A(r) \sin^2 i_0 + r(1 + 3 \cos^2 i_0)}{4}, \quad D_2(r) = \frac{\sin i_0 \cos i}{2} [rA(r)h_0(r) + h_0(r) + rh'_0(r)], \quad (\text{A12})$$

$$D_3(r) = - \frac{r(rA(r) + 1) \sin^2 i_0}{4}, \quad E_0(r) \equiv -r \cos i_0 \cot i, \quad E_1(r) \equiv - \frac{rh'_0(r) \cos i_0}{2}, \quad (\text{A13})$$

$$F_0(r) \equiv \left[\frac{3h_0(r)r \cos i_0}{2(r^2 + h_0^2(r))} \right], \quad F_1(r) \equiv \left[\frac{3h_0(r)h'_0(r) \sin i_0}{2(r^2 + h_0^2(r))} \right]. \quad (\text{A14})$$

A.3. Fourier decomposition of the velocity residual

The Fourier expansion for Equation (69) is

$$(-1)^{\varepsilon+1} \frac{\delta v_{\text{res,depro}}(r, \phi) \Delta(r, \phi)}{V_{K,0}(r)} = G_0(r) + G_1(r) \cos \phi + G_2(r) \cos 2\phi + G_3(r) \cos 3\phi \quad (\text{A15})$$

$$+ H_1(r) \sin \phi + H_2(r) \sin 2\phi + H_3(r) \sin 3\phi, \quad (\text{A16})$$

where

$$\begin{aligned} G_0(r) &= D_0(r) \delta \text{PA}, \\ G_1(r) &= F_0(r) \delta h + [C_0(r) + E_0(r)] \delta i, \\ G_2(r) &= D_2(r) \delta \text{PA}, \\ G_3(r) &= C_2(r) \delta i, \\ H_1(r) &= D_1(r) \delta \text{PA}, \\ H_2(r) &= [B_0(r) + F_1(r)] \delta h + [C_1(r) + E_1(r)] \delta i, \\ H_3(r) &= D_3(r) \delta \text{PA}. \end{aligned}$$

REFERENCES

- Aizawa, M., Muto, T., & Momose, M. 2024, MNRAS, 532, 1361, doi: [10.1093/mnras/stae1549](https://doi.org/10.1093/mnras/stae1549)
- Benisty, M., Stolker, T., Pohl, A., et al. 2017, A&A, 597, A42, doi: [10.1051/0004-6361/201629798](https://doi.org/10.1051/0004-6361/201629798)
- Casassus, S., & Pérez, S. 2019, ApJL, 883, L41, doi: [10.3847/2041-8213/ab4425](https://doi.org/10.3847/2041-8213/ab4425)
- Casassus, S., Marino, S., Pérez, S., et al. 2015, ApJ, 811, 92, doi: [10.1088/0004-637X/811/2/92](https://doi.org/10.1088/0004-637X/811/2/92)
- Izquierdo, A. F., Testi, L., Facchini, S., Rosotti, G. P., & van Dishoeck, E. F. 2021, A&A, 650, A179, doi: [10.1051/0004-6361/202140779](https://doi.org/10.1051/0004-6361/202140779)
- Izquierdo, A. F., Stadler, J., Galloway-Sprietsma, M., et al. 2025, ApJL, 984, L8, doi: [10.3847/2041-8213/adc439](https://doi.org/10.3847/2041-8213/adc439)
- Law, C. J., Teague, R., Loomis, R. A., et al. 2021, ApJS, 257, 4, doi: [10.3847/1538-4365/ac1439](https://doi.org/10.3847/1538-4365/ac1439)
- Law, C. J., Crystian, S., Teague, R., et al. 2022, ApJ, 932, 114, doi: [10.3847/1538-4357/ac6c02](https://doi.org/10.3847/1538-4357/ac6c02)
- Longarini, C., Lodato, G., Rosotti, G., et al. 2025, ApJL, 984, L17, doi: [10.3847/2041-8213/adc431](https://doi.org/10.3847/2041-8213/adc431)
- Öberg, K. I., Guzmán, V. V., Walsh, C., et al. 2021, ApJS, 257, 1, doi: [10.3847/1538-4365/ac1432](https://doi.org/10.3847/1538-4365/ac1432)
- Orihara, R., & Momose, M. 2025, ApJ, 986, 215, doi: [10.3847/1538-4357/add890](https://doi.org/10.3847/1538-4357/add890)
- Pineda, J. E., Quanz, S. P., Meru, F., et al. 2014, ApJL, 788, L34, doi: [10.1088/2041-8205/788/2/L34](https://doi.org/10.1088/2041-8205/788/2/L34)
- Pinte, C., Price, D. J., Ménard, F., et al. 2018a, ApJL, 860, L13, doi: [10.3847/2041-8213/aac6dc](https://doi.org/10.3847/2041-8213/aac6dc)
- Pinte, C., Ménard, F., Duchêne, G., et al. 2018b, A&A, 609, A47, doi: [10.1051/0004-6361/201731377](https://doi.org/10.1051/0004-6361/201731377)

- Pinte, C., Price, D. J., Ménard, F., et al. 2020, ApJL, 890, L9, doi: [10.3847/2041-8213/ab6dda](https://doi.org/10.3847/2041-8213/ab6dda)
- Rosenfeld, K. A., Chiang, E., & Andrews, S. M. 2014, ApJ, 782, 62, doi: [10.1088/0004-637X/782/2/62](https://doi.org/10.1088/0004-637X/782/2/62)
- Stadler, J., Benisty, M., Winter, A. J., et al. 2025, ApJL, 984, L11, doi: [10.3847/2041-8213/adb152](https://doi.org/10.3847/2041-8213/adb152)
- Stapper, L. M., Hogerheijde, M. R., van Dishoeck, E. F., & Paneque-Carreño, T. 2023, A&A, 669, A158, doi: [10.1051/0004-6361/202245137](https://doi.org/10.1051/0004-6361/202245137)
- Teague, R., Bae, J., & Bergin, E. A. 2019, Nature, 574, 378, doi: [10.1038/s41586-019-1642-0](https://doi.org/10.1038/s41586-019-1642-0)
- Teague, R., Benisty, M., Facchini, S., et al. 2025, ApJL, 984, L6, doi: [10.3847/2041-8213/adc43b](https://doi.org/10.3847/2041-8213/adc43b)
- Wagner, K., Apai, D., Kasper, M., & Robberto, M. 2015, ApJL, 813, L2, doi: [10.1088/2041-8205/813/1/L2](https://doi.org/10.1088/2041-8205/813/1/L2)
- Winter, A. J., Benisty, M., Izquierdo, A. F., et al. 2025, preprint, arXiv:2507.11669
- Zuleta, A., Birnstiel, T., & Teague, R. 2024, A&A, 692, A56, doi: [10.1051/0004-6361/202451145](https://doi.org/10.1051/0004-6361/202451145)